

Target and detection techniques for the $^{13}\text{N}(p,\gamma)^{14}\text{O}$ reaction using radioactive ion beams: $^{13}\text{C}(p,\gamma)^{14}\text{N}$ reaction as a test case

W. Galster, P. Leleux, I. Licot, E. Lienard, P. Lipnik, D. Mertens,
 T. Delbar, and J. Vervier

Institut de Physique Nucléaire, Université Catholique de Louvain, Louvain-la-Neuve, Belgium

P. Decrock, M. Huyse, and P. Van Duppen

Instituut voor Kern-en Stralingsfysika, Katholieke Universiteit Leuven, Leuven, Belgium

P. Duhamel and J. Vanhorenbeeck

Institut d'Astronomie, d'Astrophysique et de Géophysique, Université Libre de Bruxelles, Bruxelles, Belgium

G. Roters, C. Rolfs, U. Schroeder, H. P. Trautvetter, and K. Wolke

Institut fuer Kernphysik, Universitaet Muenster, Muenster, Germany

J. Lambert and W. S. Rodney

Physics Department, Georgetown University, Washington, D.C. 20057

(Received 21 June 1991)

A feasibility study was undertaken for the measurement of the resonance at $E_r=545$ keV in the $^{13}\text{N}(p,\gamma)^{14}\text{O}$ reaction, using intense radioactive ion beams. The analog resonance at $E_r=512$ keV in $^{13}\text{C}(p,\gamma)^{14}\text{N}$ was chosen as a test case, leading to improved knowledge of the resonance parameters. Thin- and thick-target yields were obtained with ^{13}C beams on an extended gas target and a polyethylene foil, respectively. In addition, thin and thick targets of enriched ^{13}C were irradiated with proton beams. Normalization problems arising with mixed ion beams ($^{13}\text{N}/^{13}\text{C}$) are discussed.

I. INTRODUCTION

In hot or explosive astrophysical scenarios, such as novae or supernovae, the temperatures are greater than 10^8 K and thus nuclear burning times can be measured in seconds or less. If the lifetime of a radioactive nucleus is longer than or of the same order as the burning time, that nucleus will be involved in the nuclear burning processes. In order to understand quantitatively the nuclear ashes produced in such scenarios, a precise knowledge of the rates (i.e., cross sections) of these reactions is needed [1]. For example, in the hot hydrogen burning CNO cycle [1,2], the first reaction involving a radioactive nucleus to become important is the reaction $^{13}\text{N}(p,\gamma)^{14}\text{O}$, with $T_{1/2}(^{13}\text{N})=10$ min.

The cross section of this reaction is expected to be dominated by the $J^\pi=1^-$ first excited state in ^{14}O at $E_x=5173\pm 10$ keV [3] corresponding to an s -wave resonance at $E_r=545\pm 10$ keV of total width [4] $\Gamma_t=38.1\pm 1.8$ keV; note that all energies are given in the center-of-mass system, unless otherwise specified. Efforts to determine the Γ_γ width of this resonance, and thus its strength, $\omega\gamma$, included first microscopic model calculations as well as indirect experimental methods ([5,6] and references therein). These efforts, however, did not provide an unique value: $\Gamma_\gamma=1.2$ to 4.1 eV, or $\omega\gamma=0.9$ – 3.1 eV.

A direct study of the reaction $^{13}\text{N}(p,\gamma)^{14}\text{O}$ required new techniques such as the availability of a ^{13}N radioac-

tive ion beam with $E_{\text{lab}}\geq 7.63$ MeV, suitable hydrogen targets and detectors. A pioneering project aimed at this study has been started recently at Louvain-la-Neuve, Belgium, using two neighboring cyclotrons, one for the ^{13}N production via the reaction $^{13}\text{C}(p,n)^{13}\text{N}$, and the other for ^{13}N acceleration. Several technical aspects of this project have been described [7,8], and the Γ_γ width of the 1^- state in ^{14}O has been recently measured [9]. As part of a continuing program, we report here on target and detection techniques. Those techniques have been tested using the analogue resonance $^{13}\text{C}(p,\gamma)^{14}\text{N}$, and they have improved substantially the information on Γ_γ and Γ_t widths for the 512 keV resonance. The expected characteristics of the ^{13}N beam are less than 1 nA particle current on the target, a beam diameter of about 10 mm near the target, an energy spread $\Delta E/E\approx 6\times 10^{-3}$, and a beam contamination with ^{13}C ions of $I(^{13}\text{C})/I(^{13}\text{N})\leq 100$ (in fact ≤ 0.01 see Ref. [9]).

The ^{13}C ions incident on a hydrogen target excite the $J^\pi=1^-$, $E_x=8062\pm 1$ keV state in ^{14}N corresponding to an s -wave resonance [3] at $E_r=512\pm 1$ keV with $\Gamma_t=30\pm 1$ keV and $\omega\gamma=9.2\pm 2.2$ eV. Other reported values for the resonance width lie in the range $\Gamma_t=30$ – 37 keV ([10–14], Table I). These values have been questioned recently [15] suggesting a revised width of $\Gamma_t=23\pm 1$ keV. The 512 keV resonance is the analogue to the one in $^{13}\text{N}(p,\gamma)^{14}\text{O}$ of present interest. Both resonances have similar values for E_r , Γ_t , and $\omega\gamma$, except for the energies of the emitted γ rays: $E_\gamma(^{13}\text{N})=5173$

TABLE I. Summary of results for the 512 keV resonance in $^{13}\text{C}(p,\gamma)^{14}\text{N}$.

Source	E_r (keV)	Γ_t (keV)	σ_r^a (mb)	$\omega\gamma^b$ (eV)
Gas target ^c				
d	511±2	36±2	1.2±0.4	7.9±2.6 ⁱ
e	509±2	34±2	1.3±0.3	7.9±2.0 ⁱ
f	509±2	35±2	1.1±0.3	6.8±1.9 ⁱ
g	512±2	33±2 ^h		
Foil target				
j	510±3	35±4	1.55±0.4 1.39±0.5	9.8±2.8 8.8±3.5
^{13}C target				
c	510.7±1.6	33.1±1.7	1.44±0.25	8.6±1.1
j	514±2.3	35.0±2.3	1.50±0.3	9.5±1.3
Previous work				
Ref. [10]	≈ 511	30.2±0.9	≈ 1.44	≈ 8.6
Ref. [11]	511±4	30±2		
Ref. [12] ^k	≈ 511	≈ 33		
Ref. [14]	517.8±0.5	37.2±0.6	0.97±0.11	8.8±1.4
Ref. [15]		23±1		
Ref. [3] ^l	512±1	30±1		9.2±2.2
Average ^m	511.5±1.2	33.8±1.2	1.32±0.2	8.5±1.2

^aTotal resonance cross section ($E = E_r$).

^bTotal resonance strength.

^cThin target experiments.

^dCapture γ rays in far geometry, small apertures, $p_t = 1$ Torr.

^eCapture γ rays in close geometry, large apertures, $p_t = 1$ Torr.

^fCapture γ rays in close geometry, large apertures, $p_t = 2$ Torr.

^gElastic scattering, small apertures, $p_t = 1$ Torr.

^hBest fit with Γ (s wave) = 26 keV and Γ (d wave) = 7 keV.

ⁱCalculated from columns 2 to 4.

^jThick-target experiment.

^kAs quoted by [13].

^lCompilation [3].

^mIn the adopted average Ref. [15] has been omitted; if it is included the average $\Gamma_t = 32.9$ keV.

keV and $E_\gamma(^{13}\text{C}) = 8062$ keV (80% branching [3]). Measurements using a ^{13}C ion beam incident on a hydrogen gas target [adapted to tandem (small apertures) and cyclotron beams (large apertures)] and a hydrated plastic foil are described in Secs. II and III, respectively. These measurements were complemented using a proton beam on a standard ^{13}C solid target (Sec. IV). In all cases the capture γ rays were observed with NaI(Tl) and/or Ge detectors. For a thin target (i.e., target thickness $\Delta \ll \Gamma_t$, as realized in the gas target setup) the resulting γ -ray yield $I_\gamma(E)$ is related to the cross section $\sigma(E)$ via the expression

$$I_\gamma(E) = N_p n_t l_\gamma \varepsilon_\gamma W(\theta_\gamma, E) \sigma(E), \quad (1)$$

where N_p is the number of incident projectiles, n_t the number of target atoms per unit volume, l_γ the effective target length seen by the γ -ray detector ($N_t = n_t l_\gamma$, number of target atoms per unit area), ε_γ the absolute γ -ray efficiency, and $W(\theta_\gamma, E)$ the known angular distribution [3]. For a thick target ($\Delta \gg \Gamma_t$, as realized in the solid target setup) the γ -ray yield is related to the resonance strength $\omega\gamma$ via

$$I_\gamma(E) = N_p \varepsilon_\gamma \frac{\lambda^2}{2} \frac{1}{\varepsilon_t} \omega\gamma, \quad (2)$$

where λ^2 is the squared de Broglie wavelength and ε_t the stopping power of the target (in the center-of-mass system). The results are compared with previous work in Sec. V. Details of all aspects of this work beyond those reported in this paper can be found in [16,17].

II. MEASUREMENTS USING AN EXTENDED GAS TARGET

A. Experimental equipment and setup

1. Accelerator

The 4 MV Dynamitron tandem accelerator at the Ruhr-Universitaet Bochum provided a ^{13}C beam between 0.7 nA and 0.8 μA particle current on the target in the energy range $E_{\text{lab}} = 6.0$ –8.5 MeV. A description of the beam properties of the accelerator has been given elsewhere [18–20] (absolute beam energy is known with a precision of $\Delta E/E = 4 \times 10^{-4}$; energy spread is less than 1 keV per unit of charge state of the incident projectile).

2. Extended gas target system and setup

Here, a windowless, differentially pumped gas target system was used [21–23]. Such systems require extremely high pumping speeds in the region of the target apertures, to ensure that the reduction in gas density from the target chamber to the region outside is as rapid as possible. Furthermore, if the background is to be kept as low as possible, the diameter of the apertures especially near the target chamber must be larger than the beam diameter (here ≥ 10 mm). In order to lower the gas pressure from about 1 Torr in the target chamber to 10^{-6} Torr outside, by taking into account the present requirements, the existing gas target system had to be extended from four to five pumping stages. A schematic diagram of the relevant parts of the present system and of the experimental setup is shown in Fig. 1 (for details, see [16,22,23]). Briefly, the beam entered a disk-shaped target chamber (20 cm diameter, 3 cm thickness, with entrance and exit pipes of 2 cm diameter) through six apertures *A* to *F*, to provide high pumping impedances. In detail, the apertures *A* to *F* had diameter/length ratios of 12/270, 20/280, 22/148, 25/280, 25/340, and 40/12 mm, respectively. The beam was stopped in a 20 W calorimeter (Sec. II B 2). The chamber had several ports radiating from the center, and the center was at a distance

$d = 229 \pm 2$ mm from the midpoint of the aperture *A*. The ports were used for several purposes [Fig. 1(a)]. The gas pressure in the target chamber (p_t) was measured with a Baratron capacitance manometer to an accuracy of $\pm 4\%$. The pressure measurement with this manometer is absolute and independent of the type of gas used. The gas pressures at several other locations in the gas target system were determined by thermocouple, Penning, and ionization gauges. For H_2 gas (99.999% chemical purity) at $p_t = 1$ Torr, the five-stage pumping system reduced the pressures to 5×10^{-2} and 8×10^{-7} Torr in the regions between the apertures *A* and *B* and *E* and *F*, respectively [Fig. 1(a)]. A similar pressure reduction was observed for other p_t values, with a maximum tolerable pressure of $p_t = 2.5$ Torr. The gas composition was monitored via elastic scattering from the target gas (Fig. 2), observed in well-collimated surface-barrier detectors (Si) placed at $\theta_{lab} = 30^\circ$ and 60° to the beam direction. Elastic-scattering yields were used throughout to monitor the combined beam intensity and target density (Sec. II B 2). In one experiment (Sec. II C), smaller dimensions for the apertures *A* and *B* were used, with diameter/length ratios of 4/12 and 3/15, respectively.

3. Gamma-ray detection

The γ -ray transitions were observed with a 10.5 cm diameter \times 10.5 cm NaI(Tl) crystal as well as with a 70% Ge detector. The detectors were placed at $\theta_\gamma = 90^\circ$, with the front face of the detectors at a distance of 2–3 cm from the beam axis [Fig. 1(b)]. The detectors were enclosed in a 5–10-cm-thick lead shield to reduce the ambient room γ -ray background as well as the beam-induced background on the beam aperture *A*, and on the beam calorimeter (the beam stop). In this setup, the target volume extended from the aperture *A* to the beam stop. Therefore, the effective target length l_γ seen by the detectors was defined by the lead shield around the detectors. This length was determined experimentally (Sec. II B 3). Due to the extended target and the close

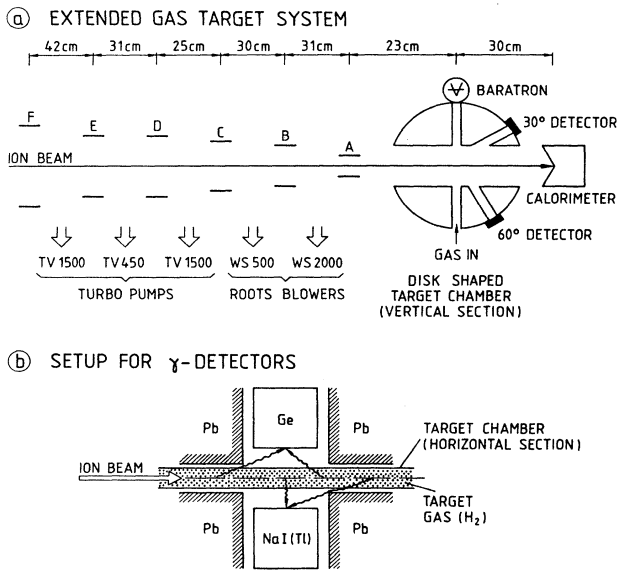


FIG. 1. Shown schematically are (a) the relevant parts of the extended gas target system and (b) the arrangement used for γ -ray spectroscopy. The beam enters the disk-shaped target chamber through apertures (*A* to *F*) and is stopped in a 20 W calorimeter. The distances between these components are also given. The target gas flowing through aperture *A* is pumped differentially with the use of Roots blowers (e.g., WS2000, pumping speed = 2000 m^3/h) and turbo pumps (e.g., TV1500, pumping speed = 1500 l/s). Well-collimated Si particle detectors placed at 30° and 60° to the beam direction were used to study elastic scattering. The effective target length seen by the γ -ray detectors is defined here by the lead collimators.

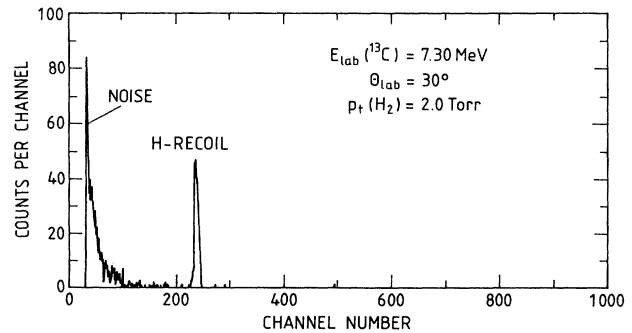


FIG. 2. Elastic-scattering spectrum obtained [in the setup of Fig. 1(a)] at $\theta_{lab} = 30^\circ$ for ^{13}C projectiles of $E_{lab} = 7.30$ MeV (0.7 nA) and $p_t (H_2) = 2.0$ Torr. The spectrum is dominated by the H-recoil nuclei. No measurable traces of gas contaminants or of contaminant ion beams are visible.

geometry of the detectors [Fig. 1(b)], the detectors observed γ -ray transitions over the angular range from $\theta_\gamma \approx 35^\circ$ to 145° . Thus, the 8.06 MeV capture γ rays exhibit substantial Doppler shifts of ± 210 keV (Fig. 4); preliminary experiments have shown that these shifts limited the advantage of high-resolution detector. For this reason, all subsequent measurements have been carried out only with the NaI(Tl) crystal.

B. Experimental procedures and data analyses

The experimental procedures and data analyses were similar to those described previously [24–26]. Therefore, only differences are discussed in the following subsections.

1. Effective beam energy

Because of the rapid pressure reduction along the beam line of the gas target system (Sec. II A 2) more than 99% of the energy loss ΔE_t of the ^{13}C beam in the target gas occurred over the distance d from the aperture A to the center of the target chamber [Fig. 1(a)]. The effective beam energy E_{eff} at the center of the target chamber is then related to the incident projectile energy E_{lab} by

$$E_{\text{eff}} = E_{\text{lab}} - \Delta E_t = E_{\text{lab}} - (p_t \varepsilon_t d), \quad (3)$$

where ε_t is the stopping power of ^{13}C projectiles in hydrogen (in units of eV/Torr cm), which is nearly constant for $E_{\text{lab}} = 6.0$ – 8.5 MeV [27]. In the case of a small aperture A (pipe of 12 mm length), the distance $d = 88$ mm could be increased at most by half the aperture's length ($= 6$ mm), if gas-blocking effects extend the gas pressure p_t up to the end of the pipe. This 7% uncertainty in d has a negligible effect on E_{eff} . However, in the case of the large aperture A (pipe of 270 mm length), the distance d could lie between 229 and 364 mm. In order to determine the actual distance d_{eff} , excitation functions of $^{13}\text{C}(p, \gamma)^{14}\text{N}$ were measured (Fig. 5 and Sec. II C) with $p_t = 1$ and 2 Torr. From the observed shift of the resonance energy, the effective distance was found to be $d_{\text{eff}} = 300 \pm 40$ mm. Quadratic addition of the uncertainties in p_t ($\pm 4\%$), ε_t ($\pm 5\%$), and d_{eff} ($\pm 13\%$) leads to an error in ΔE_t of $\pm 14\%$. For example, with $p_t = 1$ Torr and $E_{\text{lab}} = 7.20$ MeV, one finds $\Delta E_t = 83 \pm 12$ keV and thus $E_{\text{eff}} = 7117 \pm 12$ keV (or $E_{\text{c.m.}} = 508.4 \pm 0.9$ keV). This procedure was used throughout the work in the determination of E_{eff} and ΔE_{eff} .

2. Current measurement

Charge-exchange effects of the incident ion beam in the gas before striking the Faraday cup make a reliable charge integration difficult, if not impossible. Instead, the elastic-scattering yields, $I_{\text{el}}(\theta_{\text{lab}})$, of the beam particles on the gas target nuclei were observed in Si detectors (500 μm thickness, 450 mm^2 active area) placed at $\theta_{\text{lab}} = 30^\circ$ and 60° [Fig. 1(a)]:

$$I_{\text{el}}(\theta_{\text{lab}}) = N_p n_t l_p d \Omega_p \left(\frac{d\sigma}{d\Omega}(\theta_{\text{lab}}) \right)_{\text{el}}, \quad (4)$$

where l_p is the effective target length seen by the Si detector, $d\Omega_p$ is the solid angle subtended by the detector, and $[d\sigma/d\Omega(\theta_{\text{lab}})]_{\text{el}}$ is the elastic-scattering cross section. The quantity n_t was calculated from p_t , corrected for the gas temperature of $20 \pm 5^\circ\text{C}$. Each Si detector was collimated by a circular aperture (30° , 3.02 ± 0.01 mm and 60° , 3.01 ± 0.01 mm diameter) and a slit aperture (30° , 2.14 ± 0.01 mm and 60° , 2.06 ± 0.01 mm width), placed at respective distances to the center of the chamber of 219 ± 2 and 215 ± 1 mm. This setup defined θ_{lab} to better than $\pm 0.5^\circ$. The 30° and 60° detectors viewed a horizontal length $l_p = 4.83 \pm 0.07$ and 2.69 ± 0.04 mm, of the extended gas target, leading to the product $l_p d\Omega_p = (7.22 \pm 0.12) \times 10^{-5}$ and $(3.98 \pm 0.06) \times 10^{-5}$ cm sr, respectively. The observed yields (Fig. 2) provide information on the product of beam intensity (N_p) and the target density (n_t) as well as on the purity of the target gas and the ion beam. This method requires an *a priori* knowledge of the elastic-scattering cross section (Fig. 3 and below).

Alternatively, the beam intensity was measured by a 20 W calorimeter [28] placed at a distance of 30 cm from the center of the target chamber. The beam is stopped in the calorimeter, where the kinetic energy E_{lab} of the projectiles is converted into heat, which is measured by the calorimeter. The total integrated beam power $L(t)$ at the calorimeter over a time period t yields the total number of the incident ions $N_p(t)$ over this time period, $N_p(t) = L(t)/E_{\text{lab}}$. This method ignores the charge state of the incident ions and, when combined with an accurate energy determination, it gives an accurate determination of the number of incident ions in a given run. The problem of heat losses, e.g., via conduction and convection transport mechanisms, has been minimized in the design of a constant temperature gradient. The 20 W calorimeter allowed for an absolute current determination to an

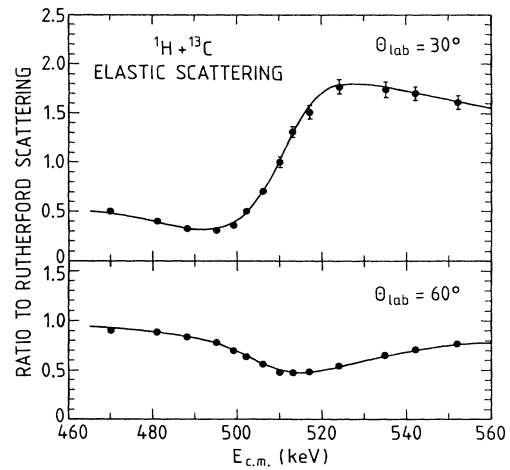


FIG. 3. The energy dependence of the elastic-scattering yields for the $^1\text{H} + ^{13}\text{C}$ system is shown relative to the Rutherford scattering law at scattering angles $\theta_{\text{lab}}(\theta_{\text{c.m.}}) = 30^\circ(120^\circ)$ and $60^\circ(60^\circ)$. The curves through the data points represent the results of fits (see Sec. II C).

accuracy of $\pm 3.0\%$ for beam powers above 1 W, i.e., for particle currents above $0.14 \mu\text{A}$ (at $E_{\text{lab}} \approx 7.0 \text{ MeV}$). The calorimeter was placed at such a distance from the target chamber that angle straggling of the beam in the gas resulted in a beam profile smaller than the 200 mm^2 active area of the calorimeter.

In one experiment, the small apertures A and B (Secs. II A 2 and II C) were used and the number of incident ^{13}C projectiles N_p was determined with the 20 W calorimeter for beam powers above 1 W. With $p_t = 1 \text{ Torr}$ the elastic-scattering cross section was calculated from the observed yields using Eq. (4). The results are shown in Fig. 3 relative to the Rutherford scattering law; they are in good agreement with previous work [12]. In other experiments, i.e., involving beam powers below 1 W, the observed elastic-scattering yields together with the data of Fig. 3 were used to determine N_p or $N_p n_t$; these values were then used in the relative and absolute normalization of the $^{13}\text{C}(p, \gamma)^{14}\text{N}$ excitation functions (Sec. II C).

3. Gamma-ray efficiency in the setup

As discussed in Sec. II A 3, the effective target length l_γ seen by the NaI(Tl) crystal was defined by the lead shield around the detector. This length was determined using a ^{22}Na source ($E_\gamma = 1.27 \text{ MeV}$), which was moved along the beam axis within the target chamber. The observed response function $\varepsilon_\gamma(b)$, where the distance scale b is measured from the center of the target chamber, could be described fairly well by a Gaussian function, where the integral over the response function could be approximated by the product $\varepsilon_\gamma(b=0)l_\gamma$. The effective target length l_γ was nearly identical with the FWHM width of the Gaussian function. One finds $l_\gamma = 13.2 \pm 0.4 \text{ cm}$ and a total absolute efficiency of $\varepsilon_\gamma(b=0) = 0.12 \pm 0.01$, both in excellent agreement with previous work [24]. The γ -ray energy dependence of l_γ , $\varepsilon_\gamma(b=0)$, and the spectrum fraction f_γ have been adopted from previous work [24]. The spectrum fraction is that part of the observed γ -ray transitions which is recorded in the portion of the spectrum from which the yield is extracted. As defined in [24] the fraction was taken to be the range $(E_\gamma - 1.5)$ to $(E_\gamma + 0.3) \text{ MeV}$ for γ -ray transitions above 4 MeV. The results have estimated accuracies of $\Delta(\varepsilon_\gamma l_\gamma) / \varepsilon_\gamma l_\gamma = \pm 10\%$ for $E_\gamma = 8 \text{ MeV}$. Alternatively, for the spectrum of the resonant γ rays (predominantly 8 MeV), the Compton plateau of the γ ray was extrapolated from about 3 MeV (Fig. 4) to zero energy using the procedure discussed in [29]. The deduced count rate together with $\varepsilon_\gamma(b=0) = 0.10 \pm 0.01$ led then to the total flux of the resonant γ rays, with an estimated error of $\pm 10\%$.

The effective target length l_γ in this close geometry of the NaI(Tl) crystal corresponds to an effective thickness, $\Delta = p_t \varepsilon_\gamma l_\gamma$, of about 36 keV for $p_t = 1 \text{ Torr}$ ($\Delta_{\text{c.m.}} = 2.6 \text{ keV}$). For comparison, the beam energy straggling (according to Bohr's formula [2]) amounts to a FWHM width of 10 keV (0.7 keV center of mass) for $d = 300 \text{ mm}$ and $p_t = 1 \text{ Torr}$.

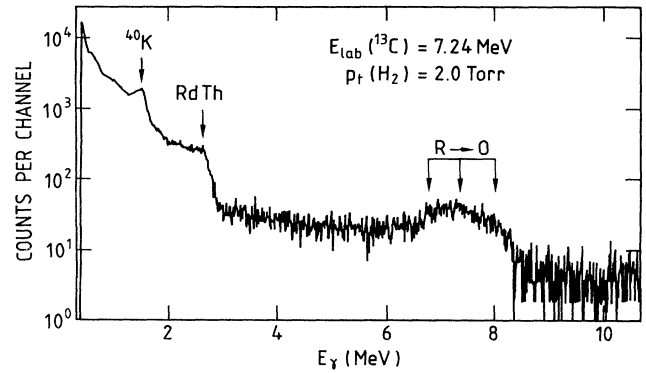


FIG. 4. Spectrum obtained with the NaI(Tl) crystal in close geometry [Fig. 1(b), large apertures] on top of the 512 keV resonance: $E_{\text{lab}}(^{13}\text{C}) = 7.24 \text{ MeV}$, $p_t(\text{H}_2) = 2 \text{ Torr}$, at a beam current of 0.7 particle nA. The $R \rightarrow O$ capture transition (80%) dominates the spectrum; due to significant Doppler shifts ($\pm 210 \text{ keV}$) the usual structures of the photopeak and single- and double-escape peaks are here not resolved. The cosmic-ray background above $E_\gamma = 8.5 \text{ MeV}$ is visible, and room background lines at low energies are identified.

In order to test the influence of the large apertures on the results for the resonant properties, measurements have also been carried out using small (standard) apertures (Sec. II A 2). In these measurements the NaI(Tl) crystal was placed in “far” geometry, i.e., at a distance of 15 cm from the beam axis, surrounded by a lead shield of 10 cm thickness with a central hole of 6.5 cm diameter [16]. Using the ^{22}Na source one finds here $l_\gamma = 8.6 \pm 0.3 \text{ cm}$ and $\varepsilon_\gamma(b=0) = (1.8 \pm 0.2) \times 10^{-2}$.

C. Results

The elastic-scattering data obtained at $\theta_{\text{lab}} = 30^\circ$ and 60° are shown in Fig. 3. The data have been fitted with the R -matrix program MULTI6 [30,31] leading to resonance parameters of $E_r = 512 \pm 2 \text{ keV}$ and $\Gamma_t = 33 \pm 2 \text{ keV}$, where the total width is composed of the partial proton width $\Gamma_p = 26$ and 7 keV for s - and d -wave formations, respectively (Table I).

The γ -ray excitation function obtained in far geometry using small apertures in the gas target system [Fig. 5(a)] has been obtained using Eq. (1) (thin-target condition) and has been fitted [16] with a single-level Breit-Wigner expression and a background amplitude arising from the direct capture process [14]. The resulting resonance parameters are summarized in Table I.

The γ -ray excitation functions obtained in close geometry using large apertures for a gas pressure of $p_t(\text{H}_2) = 1.0$ and 2.0 Torr are shown in Figs. 5(b) and 5(c), respectively. Using the same analyses procedures as just discussed, the resulting resonance parameters are also given in Table I.

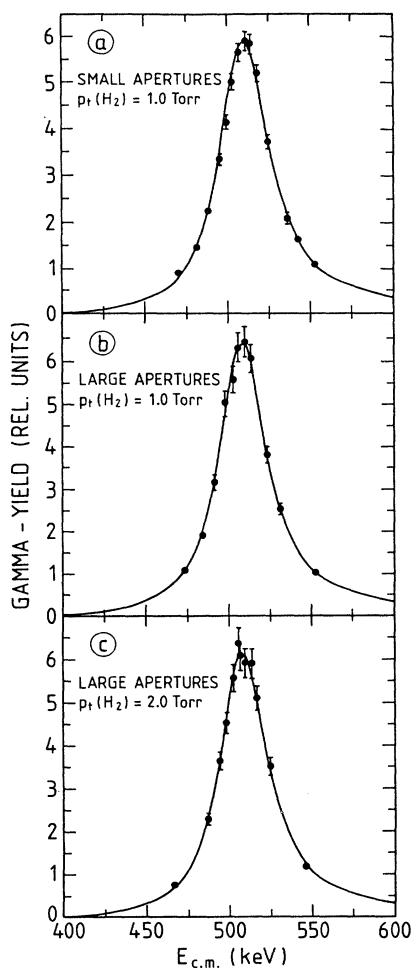


FIG. 5. Excitation functions for the 512 keV resonance of $p(^{13}\text{C}, \gamma)^{14}\text{N}$ as obtained in the setups with (a) small apertures and $p_i(\text{H}_2) = 1$ Torr, (b) large apertures and $p_i(\text{H}_2) = 1$ Torr, and (c) large apertures and $p_i(\text{H}_2) = 2$ Torr. The curves through the data points are the results of fits.

III. MEASUREMENTS USING A FOIL TARGET

A. Experimental equipment and setup

1. Reaction chamber and detection setup

A reaction chamber has been built for detection of γ rays in a highly radioactive environment. The chamber houses the solid target, the Pb shields, and the detectors for on-line monitoring of the target thickness and the beam composition ($^{13}\text{N}/^{13}\text{C}$). The solid target assembly consists of a self-supporting polyethylene foil mounted on a rotating annulus (inner diameter of 280 mm) driven by a variable speed motor at its circumference. The general layout with some details of the rotating target is displayed in Fig. 6. The modular design comprises three parts, each of which can be independently adapted to specific requirements.

(1) The frontal part includes the rotating target, the viewports for six $7.62\text{ cm} \times 7.62\text{ cm}$ NaI(Tl) crystals or alternatively four (70–90%) Ge detectors, and the Teflon-insulated transition pipe to the beam line. Being very close to the target, the NaI(Tl) or Ge detectors cover 40% or 25% of the backward hemisphere; note that the forward hemisphere lies in the domain of the elastically scattered radioactive ions.

(2) The central part contains the Pb shields that should reduce the count rate from annihilation gammas to $\leq 15 \times 10^3$ counts/sec per detector per 1 particle nA of radioactive beam. Six ports perpendicular to the beam axis located 110 and 275 mm behind the plastic target, respectively, are used for beam diagnosis: (a) a retractable quartz and Faraday cup; (b) a retractable transport tape to monitor the beam activity; and (c) two Si detectors at $\theta_{\text{lab}} = 18^\circ$ and 28° for the measurement of recoiling protons and the elastically scattered events on carbon.

(3) The rear section serves as a Faraday cup. The radioactive beam is stopped at the end of a 1500-mm-long pipe, in order to reduce the effective detector solid angle for annihilation gammas.

The entire chamber assembly is electrically insulated from the beam line. It has an inner diameter of 300 mm and an overall length (without Faraday cup) of 500 mm. The pilot experiment $^1\text{H}(^{13}\text{C}, \gamma)^{14}\text{N}^*$ described here was also carried out at the Bochum Tandem Dynamitron. The γ rays were detected by means of a 70% Ge and $7.62 \times 7.62\text{ cm}^2$ NaI(Tl) counter. Even though there was a Doppler shift of about 100 keV using a foil target, the best results were obtained with the Ge detector.

2. Foil target

For foil targets containing hydrogen one may choose either various plastics or hydrogen-implanted backings. In the implanted targets the backing must be kept at a minimum to reduce multiple scattering of the incident radioactive ion beam; this leads to a low hydrogen concentration. Among the plastics all those which contain heavy atoms such as N, O, Cl, etc., lead to backscattering of the ^{13}N beam, causing a high activity close to the γ detectors. Thus one is limited to the use of pure hydrocarbons of the type $(\text{CH}_2)_n$.

The commercially available polymers with pure hydrocarbon chains are polyethylene (PE), polypropylene (PP), and polyisobutylene (PI). Polypropylene can be stretched to thin foils of $\leq 200\text{ }\mu\text{g}/\text{cm}^2$ with ease. The resulting films are rather homogeneous and strong. PP does withstand irradiation with lowly ionizing particles (p, d, α) of several tens of particle nA. However, thin PP foils are readily destroyed through irradiation by highly ionizing heavy ions of low intensities (1–3 particle nA). In test runs static PP foils of $100\text{--}200\text{ }\mu\text{g}/\text{cm}^2$ were exposed to ^{13}C beams to 8 MeV and 1–3 particle nA: a rapid loss of hydrogen and carbon was observed in the monitor counter, followed by rupture after a few tens of seconds.

Through a viewport it was seen that under irradiation a strong tension builds up in the center, eventually tearing a hole in the foil rather than melting it. Slackening the foils and defocusing the beam brought only minor im-

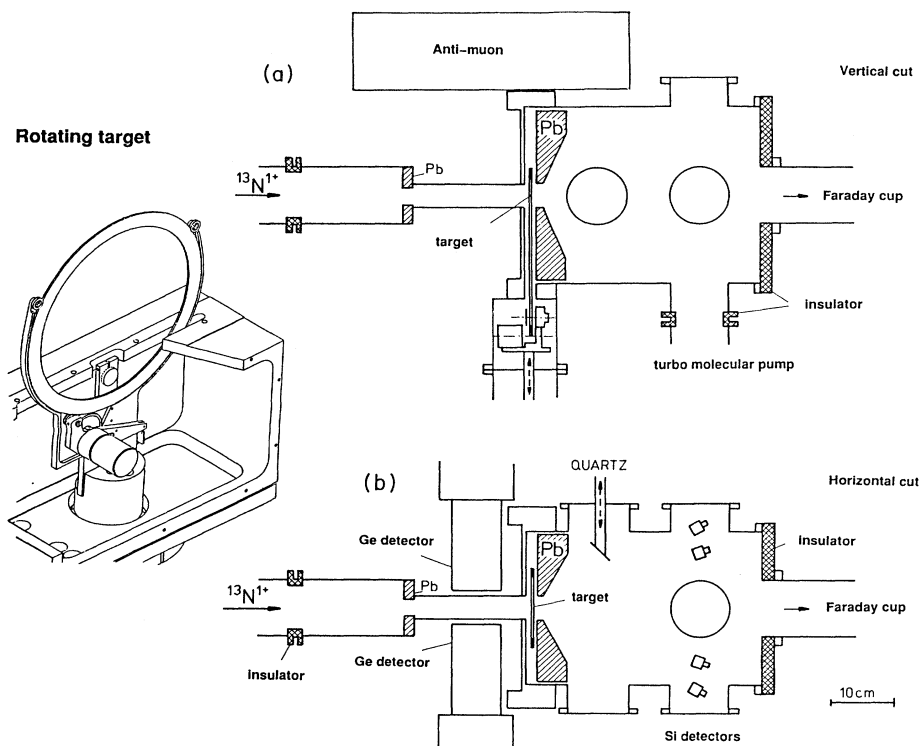


FIG. 6. The reaction chamber used in the foil target experiments. Vertical cuts parallel and perpendicular to the beam direction are shown. The ports have inner diameters of 100 mm and all flanges are interchangeable. The positions of the monitor detectors for recoil proton and elastically scattered heavy ions, and for target thickness monitoring by means of an Am- α source, respectively, are indicated. The cut away section shows details of the rotating target.

provements. To enhance the thermal conductivity 10–20 $\mu\text{g}/\text{cm}^2$ of Al were evaporated on both sides of some PP foils. These Al-PP-Al sandwich targets did not develop holes, but experienced the same rates of loss in hydrogen and carbon as pure PP foils.

Thin films of polyethylene provided by UCB-GENT [32] were less homogeneous, softer, and considerably weaker than PP foils. Tests showed that PE is more resistive to radiation damage and exhibits “healing” properties: a steady loss of hydrogen was observed, but the carbon content of the film remained constant; the beam intensity (^{13}C , 8 MeV) could be gradually increased to 60 particle nA, without destroying the foil. This conditioning up to high intensities results in the transformation of PE into a pure carbon foil of good strength and homogeneity.

The different behavior of PP and PE under irradiation can be understood as follows: (i) the energy loss of the heavy ions results in the ionization of molecules leading to chemical transformations in the polymer; (ii) the main chemical transformations are the emission of hydrogen and methane, the cross-linking between chains, the recombination of chain ends (=healing) and the degradation (=chain scission); (iii) PE exhibits cross-linking and healing following the emission of hydrogen, if it is conditioned carefully—PP suffers strong degradation following the loss of hydrogen and methane.

The branching in the main chain H-C-CH₃ introduces weak points into the polymer structure. From this it is clear that polyisobutylene will be the least resistive to irradiation among the three plastics. Chemical modifications in irradiated polymers due to x rays, γ rays, and fast electrons have been discussed by Chapiro [33]. The author limits his discussion to low-energy densities. We find the same mechanisms at work at the high-energy densities deposited by light heavy ions (^{13}C). It was concluded that PE is superior to PP as target material. Spread out over an annulus of a slowly (≈ 1 revolution/sec) rotating target, the loss of the hydrogen in the target was estimated to be about 0.5% per particle nA per hour. These expectations were verified in the experiments described here.

B. Experimental procedures and data analyses

Only the spectra obtained with the 70% Ge detector are discussed here. The spectra obtained with the NaI(Tl) were comparable to the ones of the gas target runs (Sec. II). The number of γ rays (I_γ) is obtained by integration of the full energy peak (I_s) after subtraction of the background (I_b) under the peak. Being practically constant above 2.6 MeV, the background is estimated by integration of an equivalent interval on the high-energy side of the full energy peak. The error of the number I_γ

takes into account the statistical errors of the two numbers I_s and I_b .

1. Gamma-ray efficiency

The absolute efficiency of the full energy peak at $E_\gamma \approx 0.4\text{--}3.2$ MeV was determined with a ^{56}Co source and a calibrated ^{152}Eu source (Fig. 7). The relative efficiency at higher energies was determined via the $^{24}\text{Mg}(p, n\gamma)^{24}\text{Al}$ reaction, using the LISOL facility [34], where the emitted γ rays of known intensities cover the energy range $1 \leq E_\gamma \leq 8$ MeV. The results were normalized to the absolute value at lower energies.

By placing the ^{152}Eu source inside and outside of the chamber under equivalent conditions (target position), the attenuation in the chamber walls was taken into account. After correction for the attenuation, the full energy peak efficiency of the Ge detector at 8 MeV is $4\pi(7.64 \pm 1.92) \times 10^{-4}$ sr.

2. Data normalization

The Γ_γ width of this resonance is derived in two independent ways: (1) by means of beam current integration using Eq. (2), which requires the knowledge of the absolute value of the target thickness; (2) the number I_γ is normalized to the resonant part of the protons $I_{p,\text{res}}$ recoiling from the target. The ratio of the γ to proton width is obtained. The latter is determined through a fit

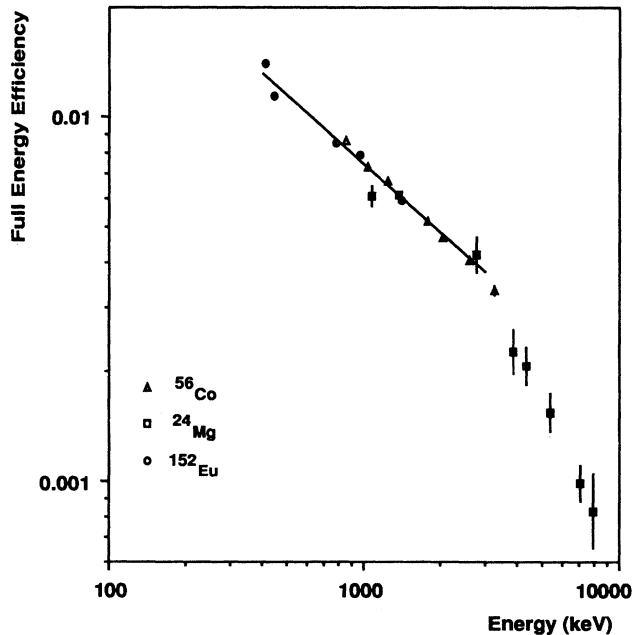


FIG. 7. Absolute efficiency of the 70% Ge detector used for $0.4 < E_\gamma \leq 8$ MeV. The quoted values are for the full energy peak only. Note the change in slope at about $E_\gamma = 3$ MeV. The total efficiency for pair production at $E_\gamma = 8$ MeV is 9 times larger than the full energy peak efficiency.

to the spectral shape of the experimental proton spectrum. The following equation is used:

$$\frac{\Gamma_\gamma}{\Gamma_p} = \frac{I_\gamma}{I_p} f_{\text{corr}} \frac{d\Omega_p}{\varepsilon_\gamma} 4 \cos\theta_L \frac{1}{b_\gamma}, \quad (5)$$

where I_p is the number of detected protons, $\Delta\Omega_p$ and θ_L are the solid angle and detection angle in the laboratory system, respectively, I_γ is the 8.06 MeV γ yield [see Fig. 8(a)] for the main branches of resonant γ rays, and $b_\gamma = 0.803$ is the γ ray branching to the ground state, the resonant yield ratio is $(I_\gamma/I_p)_{\text{res}} = (I_\gamma/I_p) f_{\text{corr}}$; the correction factor is evaluated through a Breit-Wigner

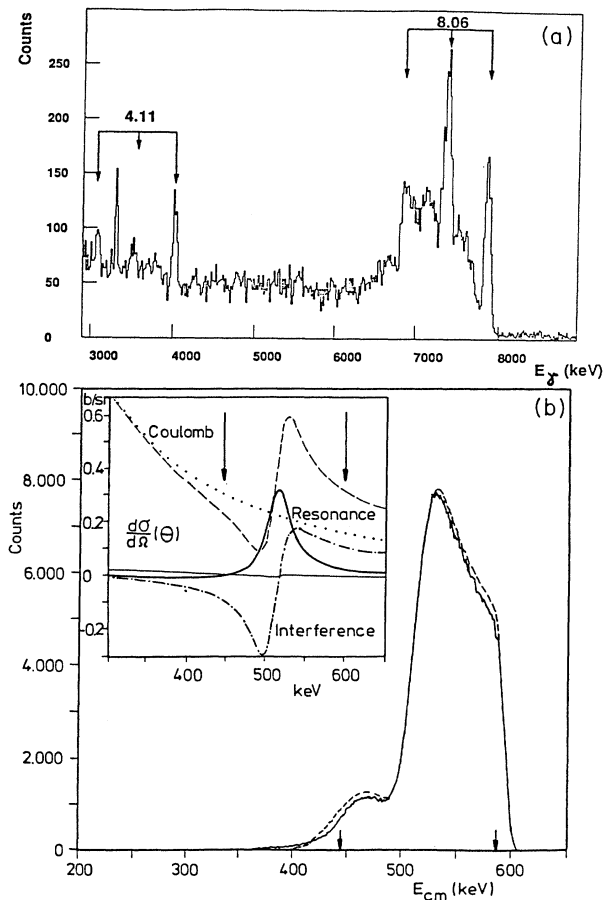


FIG. 8. Spectra of γ rays and recoil protons at $E_{\text{lab}}(^{13}\text{C}) = 8.0$ and 8.3 MeV, respectively. (a) The γ spectrum is dominated by the decays to the ground state ($E_\gamma = 8.06$ MeV, 80.3%) and to the 1^+ state at 3.95 MeV ($E_\gamma = 4.11$ MeV, 12.7%); the full energy, single- and double-escape peaks are marked by arrows. (b) The proton spectrum transformed to the c.m. system exhibits a characteristic pattern due to interference of resonance and Coulomb amplitudes. The arrows indicate the energy centroids of the ^{13}C beam incident on and emerging from the thick target. The fit (dashed line) is based on a Breit-Wigner analysis, whose different components are shown in the inset, the energy range between the arrows is scanned in the thick target.

analysis. The latter procedure offers the advantage of avoiding systematic errors inherent in the determination of the target thickness and the beam current integration.

For proton counting a silicon detector is placed behind the target at $\theta_L = 17.8 \pm 0.3^\circ$ ($\theta_{c.m.} = 144.4 \pm 0.6^\circ$) with respect to the beam. The effective solid angle of the Si detector was $d\Omega = (1.66 \pm 0.12) \times 10^{-3}$ sr. Figure 8(b) exhibits the proton yield at $\theta_{c.m.} = 144.4^\circ$ in the center-of-mass frame. The dashed line is a fit based on a Breit-Wigner analysis, whose components are displayed in the inset. The arrows at higher energy indicate the mean energy of the incident beam ($E_L = 8.3$ MeV), while the arrows at lower energy correspond to the mean energy of the ^{13}C ions emerging from the target. The region in between the arrows corresponds to the energy range scanned by the protons recoiling from the target.

These recoiling protons are essentially due to Coulomb scattering (dotted), resonant scattering (full line), and interference (dash-dotted) of these two amplitudes; the thin line reflects the sum of the hard sphere scattering and of its respective interference terms. The resulting excitation function is shown by the dashed line and clearly exhibits an interference structure. This interference pattern can be seen in the thick-target proton yield in Fig. 8(b). Note that the peak on the right-hand side depends only on the beam energy, beam spread, and resonance parameters E_r , $\Gamma_i \simeq \Gamma_p$, as long as the target thickness $\Delta \gg \Gamma_i$. The low-energy part contains the effects of thickness inhomogeneities and energy-loss straggling in the target. Consequently, the analysis is concentrated on a proper evaluation of the large peak on the right-hand side in Fig. 8(b).

The ^{13}C beam of incident energy E_0 loses a fraction ΔE of its energy when it passes through the target. This energy loss is a function of the target thickness. The proton cross section in the energy range E_0 and $E_0 - \Delta E$ [see inset of Fig. 8(b)] is converted into a simulated proton spectrum (dashed line), by taking into account the energy spread of the beam, the intrinsic resolution, and the angular range of kinematical acceptance of the detector. After transformation into the c.m. frame with a factor $(4 \cos \theta_L)$, the experimental spectra are fitted to extract the resonance parameters E_r , Γ_i . The sharp decline in the central region of the spectra is most sensitive to the resonance parameters E_r , Γ_i ; the high-energy side (upper arrow) contains information on the absolute beam energy and its dispersion. The correction factor f_{corr} is given by the ratio between the integrals of the resonant Breit-Wigner part and the total cross section in the integration region. Both γ and proton counts are corrected for the finite size of the integration interval. Full details of the analysis will be given in a forthcoming publication [35].

3. The thickness of the target

The average thickness and homogeneity of the polyethylene target was obtained from the total γ intensity measured at different beam energies. Figure 9 shows the γ intensity as a function of the ^{13}C beam energy. The beam energy was varied from $E_L = 6$ to 10 MeV in steps

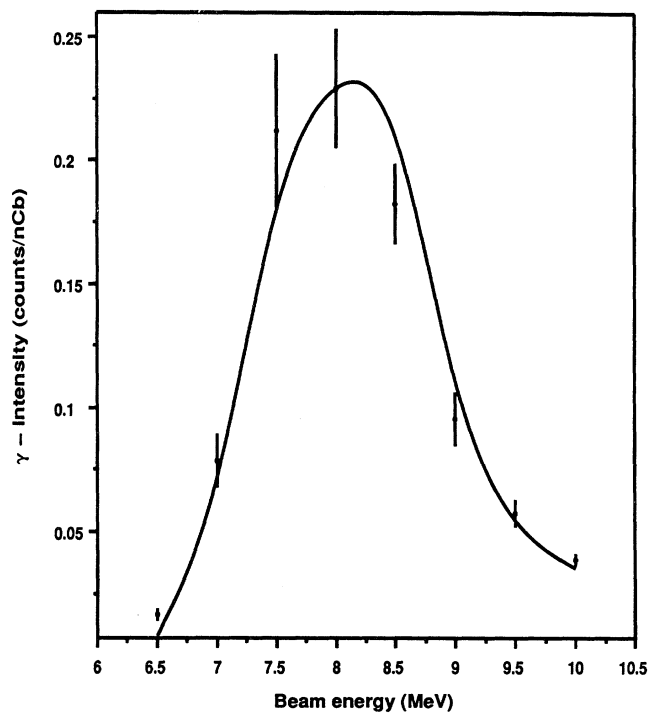


FIG. 9. Thick-target yield excitation function for $p(^{13}\text{C}, \gamma)$; the intensities reflect the total cross section for pair production. For details see text.

of 0.5 MeV. The experimental points correspond in fact to the integration of the Breit-Wigner expression in the energy range covered by the thick target. The asymmetry of the curve on the right-hand side arises from the Coulomb correction of the energy-dependent penetrability and from the inhomogeneity of the target. The fit in Fig. 9 is obtained through integration of the Lorentzian over the target and includes the Coulomb corrections only. The average thickness before irradiation was measured with an Am- α source to be about $230 \mu\text{g}/\text{cm}^2$, decreasing to $150 \mu\text{g}/\text{cm}^2$ after 11 hours of irradiation. After an initial period of irradiation, a ring-shaped track is clearly visible on the rotating target. The target thickness decreases drastically by $\sim 30\%$ during the first hour of irradiation through stretching and the target becomes more homogeneous afterwards ($175 \pm 17 \mu\text{g}/\text{cm}^2$). This effect can be seen in Fig. 10, where the curves represent the numbers of scattered protons I_p , scattered carbon atoms I_C , and I_γ , respectively, normalized to the beam intensity I_b as a function of the irradiation time. After ~ 1 hour the ratio I_C/I_b stays constant; after the initial stretching, the number of carbon atoms in the target remained constant during 11 hours of irradiation. The ratio I_p/I_b also decreases rapidly during the first hour of irradiation, but later on the target loses only a small fraction of its protons. The observed loss in hydrogen was about 16% during the last 10 hours of irradiation with 3 particle nA of ^{13}C beam (0.5% per hour per particle nA).

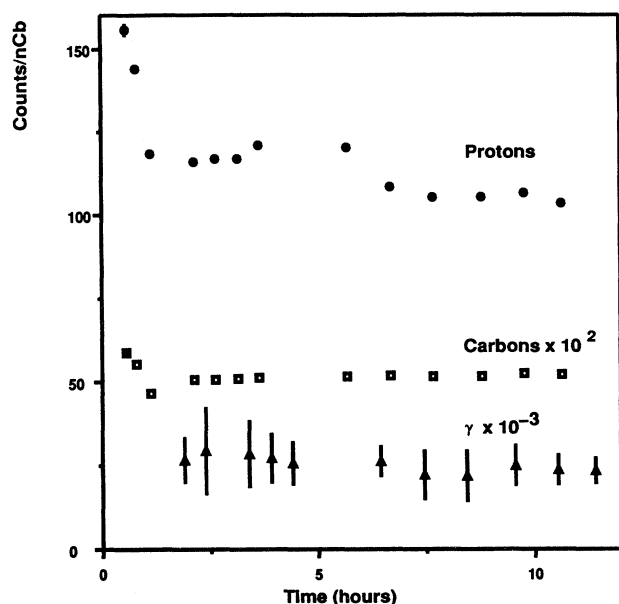


FIG. 10. Measured yields at $E_{\text{lab}}(^{13}\text{C})=8.0$ MeV as a function of running time. The normalized yields for recoil protons N_p , elastically scattered ^{13}C on ^{12}C (CH_2 target) N_C , and γ rays N_γ are displayed. Note the constancy of N_C and N_γ ; N_γ reflects the full energy peak only.

4. Results and discussion

The thick-target yield as a function of beam energy is shown in Fig. 9. The maximum γ yield is obtained at $E_L=8$ MeV and, consequently, this energy was chosen for the measurement of the width Γ_γ ; the data were checked frequently (see Fig. 10). The energy E_r and total width Γ_t of the resonance were extracted from Fig. 9. For an infinitely thick target, E_r and Γ_t correspond to 50% and to the difference between 25% and 75% of the saturation yield, respectively. The correction for finite target thickness Δ is obtained through

$$\left(\frac{I_\gamma^\Delta}{I_\gamma} \right) = \frac{2}{\pi} \arctan \left(\frac{\Delta}{\Gamma_t} \right). \quad (6)$$

The same information on E_r and Γ_t is also obtained from the shape of the spectra of the recoiling protons, by means of the procedure described in Sec. III B 2. Analogous to the thick-target γ yield, the measurement of the thick-target proton yield is equivalent to a thin-target excitation function. In particular at forward angles, the pronounced spectral shape arising from the interference between the resonant and the Coulomb part is evident (compare Figs. 2 and 8) and allow for the determination of E_r and Γ_t . The results are summarized in Table I. The first and second rows of the foil target values correspond to the beam integration and the proton normalization, respectively. The quoted absolute errors are largely due to uncertainties in the efficiency calibration of the Ge detector ($\pm 25\%$). In the case of $p(^{13}\text{C},\gamma)$ the absolute normalization using a Faraday cup invokes smaller errors

than the more complex proton normalization. However, the situation will be reversed, when a contaminated radioactive ion beam is used ($^{13}\text{N}/^{13}\text{C}$). The activity can be measured directly using NaI(Tl) and/or β scintillators, but this also involves substantial errors. Consequently, both methods have been used for $p(^{13}\text{N},\gamma)$, as it is always desirable to use two independent means.

IV. MEASUREMENTS USING A PROTON BEAM

To supplement the results (Table I) just described, we have also investigated the $E_r=512$ keV resonance using normal kinematics $^{13}\text{C}(p,\gamma)^{14}\text{N}$. Since Doppler shifts and broadening are significantly reduced, the structure in the γ -ray spectrum near $E_\gamma(^{13}\text{N})=5.17$ MeV (Sec. I) was studied in detail.

A. Experimental setup

The proton beam of about $1 \mu\text{A}$ was provided by the 4 MeV Van de Graaff accelerator at the LARN Institute (Namur, Belgium). The absolute energy and the energy spread of the beam was about 1 keV. For the thin-target measurements the energy was varied in the range $460 \leq E_p \leq 640$ keV in steps of 5 keV. The thick-target experiment was carried out at $E_p=640$ keV. Self-supporting ^{13}C targets enriched to 98% were used; the thickness was 440 ± 40 and $10.7 \pm 1 \mu\text{m}/\text{cm}^2$ for the thick and the thin target, respectively. The 70% Ge detector (Sec. III) was positioned at a distance of 100 mm and at $\theta_\gamma=90^\circ$ to the beam direction. The stability of the electronics, the pile-up rate, and the dead time were controlled by means of a calibrated pulse generator. The beam energy current was determined in a suppressed Faraday cup placed at 1.50 m from the target.

B. Data analysis

For the thin target ($\Delta \sim \frac{1}{6}\Gamma_t$) the energy region of the resonance was investigated. The full energy peak at $E_\gamma \approx 8$ MeV was fitted with a Lorentzian superimposed on a linear background. The resulting excitation function is shown in Fig. 11, where the line through the data points represents a fit including the usual energy dependence of partial and total widths.

In the thick-target measurements ($\Delta \approx 7\Gamma_t$) the energy of the incident proton beam was chosen such as to have the resonance energy E_r in the center of the target. After correcting for the resolution and Doppler shift and broadening of the detector, the resonance energy and the total width are obtained directly from a fit to the spectral shape of the γ spectrum. The thick-target yield spectrum is equivalent to the excitation function obtained with the thin target. In Fig. 12 γ -ray spectra obtained with the thin and thick targets, respectively, are shown.

C. Results and discussion

The results of the thin and thick target measurements are compiled in Table I. The values obtained are consistent with those from the experiments using an extend-

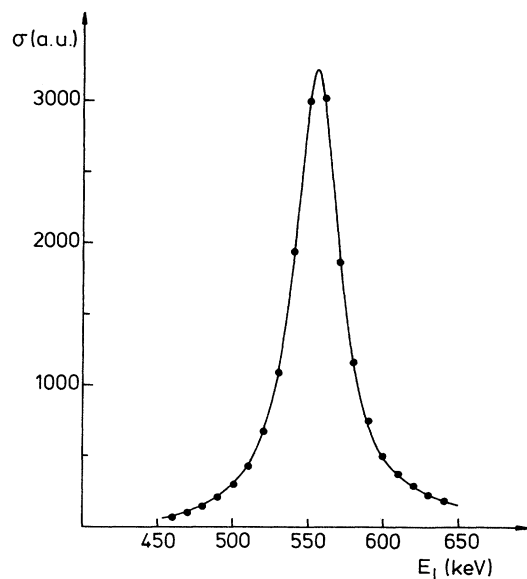


FIG. 11. Thin-target excitation function of the $E_r = 512$ keV resonance of $^{13}\text{C}(p, \gamma)^{14}\text{N}$ obtained with normal kinematics. The Lorentzian fit includes the Coulomb corrections for the energy-dependent penetrability.

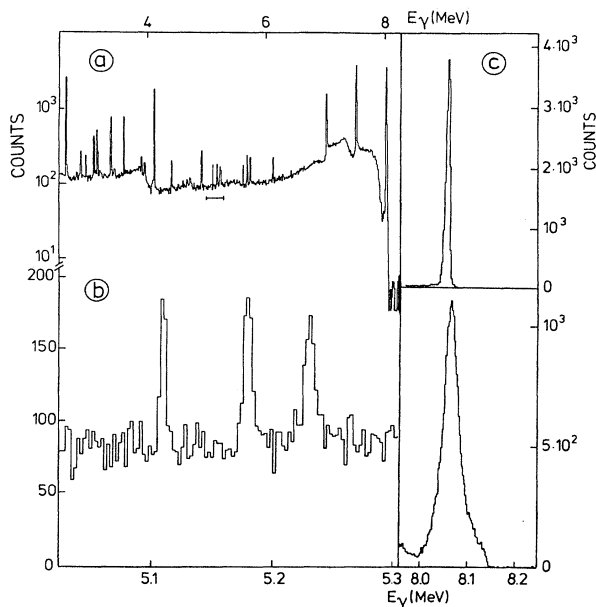


FIG. 12. Ge spectra for thin and thick ^{13}C targets: (a) Thin-target spectrum $2.5 \leq E_\gamma \leq 8.5$ MeV; the full energy peak of the capture γ ray is seen at $E_\gamma = 8.06$ MeV. (b) Expanded region around $E_\gamma \approx 5$ MeV. (c) Full energy peak of the capture γ ray for the thin (upper) and thick targets (lower).

ed gas target and a thick foil target, respectively.

The second objective was to examine the γ background around $E_\gamma \approx 5$ MeV. It is obvious from Fig. 12 that some contaminant γ rays are seen, which can effect the detection of the 5.17 MeV γ ray from the first excited level in ^{14}O (Sec. I). The decay of the 1^- level in ^{14}N at 8.06 MeV is governed by the γ transition to the 1^+ ground state (80.3%), but γ rays resulting from transitions to excited states cannot be neglected. The transition to the first excited 0^+ state at 2.31 MeV results in $E_\gamma = 5.75$ MeV; its first escape peak appears at 5.24 MeV, very close to 5.17 MeV ^{14}O line. A comparison of the thin- and thick-target yields reveals that it is a direct γ transition; the thick-target spectrum is Doppler broadened (Fig. 12). Even more troublesome is the indirect cascade transition from the 1^- level at 5.69 MeV; its first escape peak appears at $E_\gamma = 5.18$ MeV. Due to the considerable Doppler broadening in the actual $p(^{13}\text{N}, \gamma)$ experiment, the first escape peaks of the γ -ray transitions at $E_\gamma = 5.69$ and 5.75 MeV would be superimposed on the ^{14}O γ ray in the Ge detectors. It was therefore necessary to reduce the ratio of $^{13}\text{C}/^{13}\text{N}$ in the beam to far below 10; otherwise, the γ spectrum would have been dominated by contributions from the $p(^{13}\text{C}, \gamma)^{14}\text{N}$ reaction.

V. SUMMARY AND CONCLUSIONS

The target and detection techniques for the study of the reaction $^{13}\text{N}(p, \gamma)^{14}\text{O}$ have been successfully tested through the measurement of the analogue resonance in $^{13}\text{C}(p, \gamma)^{14}\text{N}$. The resonance parameters of the latter have been determined with improved precision, using three independent techniques. In reverse kinematics, ^{13}C beams were used to bombard an extended gas target (thin-target yield) and a polyethylene foil target (thick-target yield), respectively. In normal kinematics, thin and thick ^{13}C targets were bombarded with proton beams. The newly recommended resonance parameters are listed in Table I.

In a first experiment, with an intense radioactive ion beam of ^{13}N , a polyethylene target, and hyperpure Ge detectors have been employed [9], using the techniques described in this report. The low efficiency for the full energy peak is partly offset by the integration over the resonance in the thick target. It is expected that the resonance parameters of $^{13}\text{N}(p, \gamma)^{14}\text{O}$ can be determined with absolute errors of $\pm 30\%$. Once the beam intensity $I(^{13}\text{N})$ has been raised to ≥ 1 particle nA, an extended gas target is of advantage; in addition, less expensive NaI(Tl) detectors can be used to enhance the detection efficiency.

Finally, we note that novel detection techniques might have to be developed to measure resonance strengths with $\omega\gamma$ proportional to a few meV, while fairly standard techniques suffice to determine $\omega\gamma$ strengths of the order of 1 eV with radioactive ion beams.

ACKNOWLEDGMENTS

The authors would like to thank M. Berheide, S. Schmidt, and M. Topheide (Muenster) for their assistance

during the course of the experiments. The help of J. Li (North Carolina State University, Raleigh) in the analysis of the elastic-scattering data is also highly appreciated. The ^{13}C targets were kindly provided by Prof. H. Voit (University of Erlangen). We would like to acknowledge the help of Prof. G. Deconninck and Prof. G. Demortier of the LARN Institute (Namur). Thanks are also due to

Dr. K. Brand (Bochum), P. Demaret (UCL), G. Lannoye (UCL), Y. Morciaux (LARN), and the workshop of UCL Louvain-la-Neuve for help during various stages of the experiments. This work was supported by DFG Grant No. Ro 429/21-1 and by a special grant from the Belgian government in the framework of the Programme of the Interuniversity Attraction Poles.

-
- [1] W. A. Fowler, *Rev. Mod. Phys.* **56**, 119 (1984).
- [2] C. Rolfs and W. S. Rodney, *Cauldrons in the Cosmos* (University of Chicago Press, Chicago, 1988).
- [3] F. Ajzenberg-Selove, *Nucl. Phys.* **A449**, 1 (1986).
- [4] T. E. Chupp, R. T. Kouzes, A. B. McDonald, P. D. Parker, T. F. Wang, and A. Howard, *Phys. Rev. C* **31**, 1023 (1985).
- [5] P. Descouvemont and B. Baye, *Nucl. Phys.* **A500**, 155 (1989).
- [6] P. B. Fernandes, E. G. Adelberger, and A. Garcia, *Phys. Rev. C* **40**, 1887 (1989).
- [7] Th. Delbar, M. Huyse, and J. Vanhorenbeeck, Belgian Interuniversity Report RIB-1988-01, 1988 (unpublished).
- [8] S. W. Kitwanga, P. Leleux, P. Lipnik, and J. Vanhorenbeeck, *Phys. Rev. C* **40**, 35 (1989); M. Arnould, F. Baeten, D. Darquennes, Th. Delbar, C. Dom, M. Huyse, Y. Jongen, M. Lacroix, P. Lipnik, M. Loiselet, G. Reusen, G. Ryckewaert, S. Wa Kitwanga, P. Van Duppen, J. Vanhorenbeeck, J. Vervier, and S. Zarembo, *Nucl. Instrum. Methods* **A282**, 99 (1989); D. Darquennes, P. Decrock, Th. Delbar, W. Galster, M. Huyse, Y. Jongen, M. Lacroix, P. Leleux, I. Licot, E. Lienard, P. Lipnik, M. Loiselet, G. Ryckewaert, S. Wa Kitwanga, P. Van Duppen, J. Vanhorenbeeck, J. Vervier, and S. Zarembo, *Phys. Rev. C* **42**, R804 (1990).
- [9] P. Decrock, Th. Delbar, P. Duhamel, W. Galster, M. Huyse, P. Leleux, I. Licot, E. Lienard, P. Lipnik, M. Loiselet, C. Michotte, G. Ryckewaert, P. Van Duppen, J. Vanhorenbeeck, and J. Vervier, *Phys. Rev. Lett.* **67**, 808 (1991).
- [10] J. D. Seagrave, *Phys. Rev.* **85**, 197 (1952).
- [11] D. F. Hebbard, Ph.D. thesis, University of Melbourne, 1957.
- [12] E. A. Milne, *Phys. Rev.* **93**, 762 (1954).
- [13] E. Kashy, R. R. Perry, R. L. Steele, and J. R. Risser, *Phys. Rev.* **122**, 884 (1961).
- [14] J. D. King, private communication.
- [15] R. A. Spits, W. Baloyi, and T. E. Derry, *Phys. Rev. C* **41**, 2429 (1990).
- [16] G. Roters, Diplomarbeit, Universitaet Muenster, 1990.
- [17] I. Licot, Ph.D. thesis, Université Catholique de Louvain, Louvain-la-Neuve, 1991.
- [18] E. Blancke, K. Brand, H. Genz, A. Richter, and G. Schreider, *Nucl. Instrum. Methods* **122**, 295 (1974).
- [19] H. P. Trautvetter, K. Elix, C. Rolfs, and K. Brand, *Nucl. Instrum. Methods* **161**, 173 (1979).
- [20] S. Wüstenbecker, H. W. Becker, C. Rolfs, H. P. Trautvetter, K. Brand, G. E. Mitchell, and J. S. Schweitzer, *Nucl. Instrum. Methods* **A256**, 9 (1987).
- [21] M. R. Dwarakanath and H. Winkler, *Phys. Rev. C* **4**, 1532 (1971).
- [22] C. Rolfs, J. Görres, K. U. Kettner, H. Lorentz-Wirzba, P. Schmalbrock, H. P. Trautvetter, and W. Verhoeven, *Nucl. Instrum. Methods* **157**, 19 (1978).
- [23] H. W. Becker, L. Buchmann, J. Görres, K. U. Kettner, H. Kräwinkel, C. Rolfs, P. Schmalbrock, H. P. Trautvetter, and A. Vlieks, *Nucl. Instrum. Methods* **198**, 277 (1982).
- [24] K. U. Kettner, H. W. Becker, L. Buchmann, J. Görres, H. Kräwinkel, C. Rolfs, P. Schmalbrock, H. P. Trautvetter, and A. Vlieks, *Z. Phys. A* **308**, 73 (1982).
- [25] H. Hilgemeier, H. W. Becker, C. Rolfs, H. P. Trautvetter, and J. W. Hammer, *Z. Phys. A* **329**, 243 (1988).
- [26] K. Wolke, V. Harms, H. W. Becker, J. W. Hammer, K. L. Kratz, C. Rolfs, U. Schröder, H. P. Trautvetter, M. Weischer, and A. Wöhr, *Z. Phys. A* **334**, 491 (1989).
- [27] F. Ziegler, *The Stopping and Ranges of Ions in Matter* (Pergamon, New York, 1980), Vol. 5.
- [28] A. Krauss, H. W. Becker, H. P. Trautvetter, C. Rolfs, and K. Brand, *Nucl. Phys.* **A465**, 150 (1987).
- [29] C. D. Zerby and H. S. Moran, *Nucl. Instrum. Methods* **14**, 115 (1961).
- [30] D. F. Fang, E. G. Bilpuch, C. R. Westerfeld, and G. E. Mitchell, *Phys. Rev. C* **37**, 28 (1988).
- [31] R. O. Nelson, E. G. Bilpuch, and G. E. Mitchell, *Nucl. Instrum. Methods* **A236**, 128 (1985).
- [32] We are grateful to U.C.B.-GENT for providing us with thin films of polyethylene.
- [33] A. Chapiro, *Nucl. Instrum. Methods* **B32**, 111 (1988).
- [34] The Leuven Isotope Separator On Line (LISOL) of the K. U. Leuven is installed at the Louvain-la-Neuve Cyclotron CYCLONE.
- [35] P. Decrock, Th. Delbar, P. Duhamel, W. Galster, M. Huyse, P. Leleux, I. Licot, E. Liénard, P. Lipnik, C. Michotte, P. Van Duppen, J. Vanhorenbeeck, J. Vervier, D. Baye, and P. Descouvemont, submitted to *Nucl. Phys.*